Nanoscale

PAPER

View Article Online
View Journal | View Issue

Cite this: *Nanoscale*, 2023, **15**, 15635

A pixelated liquid perovskite array for high-sensitivity and high-resolution X-ray imaging scintillation screens†

Mingzhu Hu,‡[a,b,c] Yumeng Wang,‡[a,b] Shengpeng Hu,‡[a,b] Zongpeng Wang,[d] Bi Du,[d] Yanjun Peng,[a,b] Jiawei Yang,[a,b] Yunjie Shi,[a] Dongdong Chen,[a,b] Xi Chen,[a,b] Ziwen Zhuang,[a] Zhixun Wang,[f] Xi Chen,[a,e] Jiecheng Yang,[g,h] Yongshuai Ge,[g,h] Eyu Wang,[i] Quan Wen,[i] Shuang Xiao,[j] Ming Ma,[a,e] Weimin Li,[a,e] Jie Zhang,[a,e] De Ning,*[a,e] Lei Wei,*[f] Chunlei Yang*[a,e] and Ming Chen*[a,e]

Scintillators with high spatial resolution at a low radiation dose rate are desirable for X-ray medical imaging. A low radiation dose rate can be achieved using a sufficiently thick scintillator layer to absorb the incident X-ray energy completely, however, often at the expense of low spatial resolution due to the issue of optical crosstalk of scintillation light. Therefore, to achieve high sensitivity combined with high-resolution imaging, a thick scintillator with perfect light guiding properties is in high demand. Herein, a new strategy is developed to address this issue by embedding liquid scintillators into lead-containing fiber-optical plates (FOPs, n = 1.5) *via* the siphon effect. The liquid scintillator is composed of perovskite quantum dots (QDs)/2,5-diphenyloxazole (PPO) and the non-polar high-refractive index (n = 1.66) solvent α-bremnaphthalene. Benefiting from the pixelated and thickness-adjustable scintillators, the proposed $CsPbBr_3$ QDs/PPO liquid scintillator-based X-ray detector achieves a detection limit of 79.1 μGy s^{-1} and a spatial resolution of 4.6 lp mm^{-1}. In addition, it displays excellent tolerance against radiation (>34 h) and shows outstanding stability under ambient conditions (>160 h). This strategy could also be applied to other liquid scintillators (such as $CsPbCl_3$ QDs and Mn:$CsPbCl_3$ QDs). The combination of high sensitivity, high spatial resolution and stability, easy fabrication and maintenance, and a reusable substrate matrix makes these liquid scintillators a promising candidate for practical X-ray medical imaging applications.

Received 14th June 2023,
Accepted 19th August 2023

DOI: 10.1039/d3nr02841k

rsc.li/nanoscale

Introduction

X-rays are an ideal radiation source for many detection applications, including medical diagnosis, defect inspection, security, and border control, benefiting from their high energy and powerful penetrating ability. Scintillator-based indirect X-ray detectors are widely used in X-ray imaging systems. Scintillation materials convert X-ray radiation into visible or ultraviolet (UV) photons, which are then absorbed by the photodetector, converted into positive and negative charges, and eventually converted into electrical signal output. Gd_2O_2S:Tb (GOS) and CsI:TI are the most commercially available scin-

[a]*Shenzhen Institute of Advanced Technology, Chinese Academy of Sciences, Shenzhen 518055, People's Republic of China. E-mail: de.ning@siat.ac.cn, cl.yang@siat.ac.cn, ming.chen2@siat.ac.cn*
[b]*Department of Nano Science and Technology Institute, University of Science and Technology of China, Suzhou 215123, People's Republic of China*
[c]*School of Microelectronics, University of Science and Technology of China, Hefei 230026, People's Republic of China*
[d]*Shenzhen Angell Technology Co. Ltd, Shenzhen 518057, People's Republic of China*
[e]*University of Chinese Academy of Sciences, Beijing 100049, People's Republic of China*
[f]*School of Electrical and Electronic Engineering, Nanyang Technological University, 50 Nanyang Avenue, 639798, Singapore. E-mail: wei.lei@ntu.edu.sg*
[g]*Paul C Lauterbur Research Center for Biomedical Imaging, Shenzhen Institute of Advanced Technology, Chinese Academy of Sciences, Shenzhen, Guangdong 518055, China*
[h]*Research Center for Medical Artificial Intelligence, Shenzhen Institute of Advanced Technology, Chinese Academy of Sciences, Shenzhen, Guangdong 518055, China*
[i]*Seamark Opticelectronic Technology (Shenzhen) Co. Ltd, Shenzhen, 518103, People's Republic of China*
[j]*Shenzhen Key Laboratory of Ultraintense Laser and Advanced Material Technology, Center for Advanced Material Diagnostic Technology, and College of Engineering Physics, Shenzhen Technology University, Shenzhen 518118, China*

†Electronic supplementary information (ESI) available: Cross-sectional SEM characterization of the LSS. Stability analysis of $CsPbBr_3$/PPO and the Mn:$CsPbCl_3$/PPO LSS under ambient moisture conditions. Light extraction efficiency of the LSS with different thicknesses under varied X-ray dose rates. See DOI: https://doi.org/10.1039/d3nr02841k

‡These authors contributed equally to this work.

tillators in indirect X-ray detectors.[1–4] However, CsI:TI is fragile and expensive, and these disadvantages make it unsuitable for application in some flexible detection scenarios, such as the commonly used oral and dental imaging.[5] GOS is relatively cost-effective and can also be combined with a flexible matrix, which broadens its application scenarios. Nevertheless, it significantly scatters the emitted light, thus reducing the spatial resolution. In addition, due to the photoluminescence (PL) delay, the response time is relatively slow.[6] Recently, inorganic perovskite quantum dots (QDs) have been regarded as potential and promising scintillation materials because of their low cost, tunable bandgap, ease of fabrication, high emission quantum yields, and high radiation resistance.[7–12]

Low-dose, high-resolution X-ray imaging is becoming more crucial in medical diagnosis.[13] A low dose can be achieved using a sufficiently thick scintillator layer to absorb the incident X-ray energy completely, however, often at the expense of low spatial resolution due to the more light scattering (Fig. 1a). Pixelated X-ray scintillators, which can trap the light by the separated individual microstructures, efficiently reduce the lateral propagation of light (Fig. 1b). Extensive efforts have been made toward fabricating pixelated scintillators.[14–18] For instance, Zhang *et al.* used the negative pressure filling method to prepare a pixelated $CsPbBr_3$-anodic aluminum oxide (AAO) scintillation screen that can realize high-resolution high-energy radiation imaging with 2 μm. The spatial resolution of the pixelated $CsPbBr_3$-AAO array scintillation screen is much higher than that of the $CsPbBr_3$ film.[17] Also, a high-resolution $Cs_3Cu_2I_5$ scintillator screen was prepared by filling the metal halide scintillators into an AAO by the hot-pressing method.[18] However, these methods are usually time-consuming and require a complicated procedure and/or cost-effective equipment. Additionally, the pixelated substrate matrix is commonly not reusable. The thickness of the scintillator is limited and non-adjustable. Compared with crystal or plastic scintillators, liquid scintillators usually have better resistance to the damage caused by exposure to strong radiation. More importantly, due to their good area/volume scalability, large areas of scintillator screens are easy to prepare for real-life scenarios. Cho *et al.* reported an efficient and low-cost scintillator consisting of perovskite QDs hybridized with the organic molecule 2,5-diphenyloxazole (PPO), and PPO could greatly improve the scintillation quantum yield.[19] However, several problems, including optical crosstalk and low sensitivity, still need to be solved.

In this work, we fabricated a liquid scintillator screen (LSS) *via* the siphon effect which was composed of a perovskite QDs/2,5-diphenyloxazole (PPO) liquid scintillator and a fiber optical plate (FOP, n = 1.5) to address the above issue. To achieve the light-guiding properties, a new solvent, α-bremnaphthalene, with a high refractive index (n = 1.66) was adopted. Benefiting from the lead-containing, thickness-adjustable fiber structure

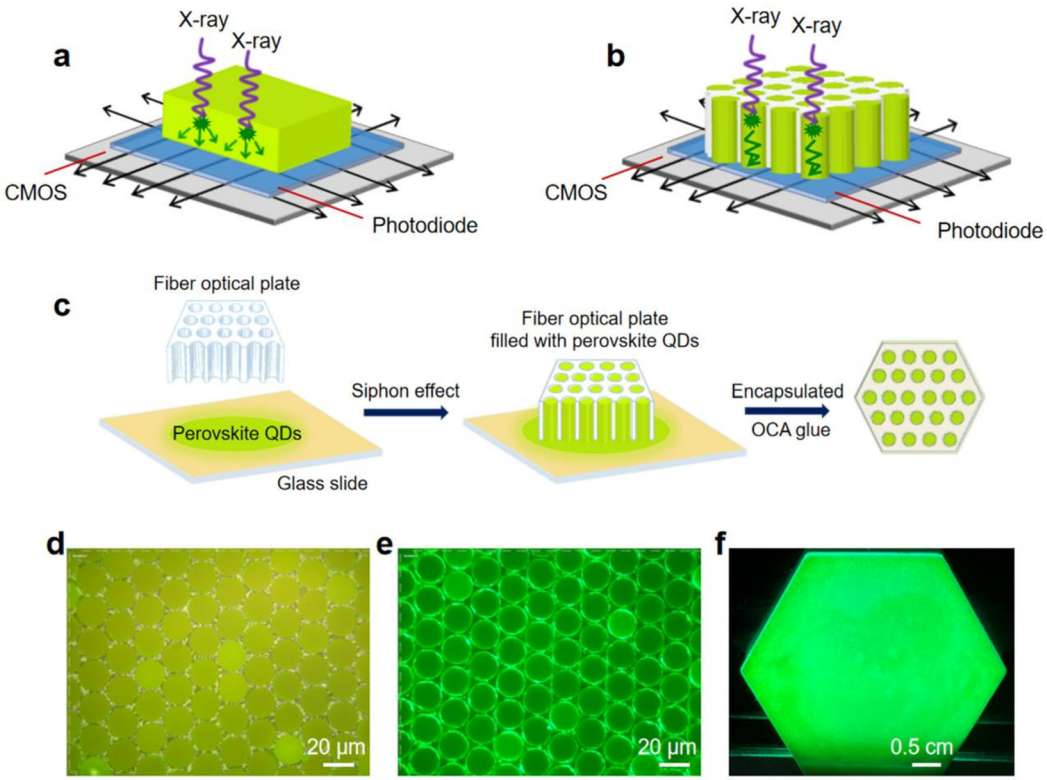

Fig. 1 (a and b) Schematic diagram of the propagation paths of scintillation light through bulk and pixelated X-ray scintillators, respectively. (c) Schematic illustration of the fabrication process of the pixelated liquid perovskite array. (d and e/f) Optical image of the pixelated $CsPbBr_3$/PPO liquid scintillator arrays under daylight and UV light excitation, respectively.

and high refractive index solvent, a detection limit of 79.1 μGy s^{-1} and a spatial resolution of 4.6 lp mm^{-1} were achieved for the $CsPbBr_3$ QDs/PPO LSS. Furthermore, the $CsPbBr_3$ QDs/PPO LSS also possessed the merits of high tolerance against radiation (>34 h) and moisture (>160 h). We also demonstrated the universality of this method in other typical perovskite scintillators, such as $CsPbCl_3$ and Mn:$CsPbCl_3$. Compared to the pixelated scintillator screen based on other filling methods, our fabrication method is facile and time-saving, as the whole filling process was achieved within several seconds. Furthermore, compared with the conventional crystal or plastic scintillators, the proposed LSS is easy to maintain, and the FOP substrate matrix is reusable. These results may lead to the development of perovskite material-based LSSs for practical X-ray imaging applications.

Results and discussion

Pixelated liquid scintillator arrays were prepared *via* the facile siphon effect, followed by the encapsulation process utilizing the commercial OCA (optically clear adhesive) glue (see Methods), as presented in Fig. 1c. Fig. 1d and e and f show the optical images of the pixelated $CsPbBr_3$/PPO liquid scintillator arrays under daylight and UV light excitation, respectively. Fig. S1† shows the cross-sectional image of the liquid scintillator arrays. The above results indicate that the liquid scintillator was filled into each columnar hole of FOP with good continuity and uniformity. The proposed strategy for the fabrication of pixelated scintillators possesses the merits of being facile, cost-effective, scalable, and widely applicable.

The $CsPbBr_3$ QDs were synthesized by the hot injection method (see Methods for details). Their transmission electron microscopy (TEM) image is shown in Fig. 2a, revealing that the $CsPbBr_3$ QDs are mostly cubic and uniformly distributed without agglomeration. The average morphological size of the prepared $CsPbBr_3$ QDs is 8.47 nm (Fig. 2b). The X-ray diffraction (XRD) pattern in Fig. 2c exhibits peaks at 15.15°, 21.58°, 25.42°, 30.68°, 34.43° and 37.85°, corresponding to the (100), (110), (111), (200), (210) and (211) crystal planes of the cubic crystal structure, and is consistent with the standard diffraction card (PDF#18-0366). Fig. S2a† shows a photograph of the organic scintillator PPO. Under X-ray irradiation, the PPO scintillator emits blue color with a peak wavelength of 400 nm

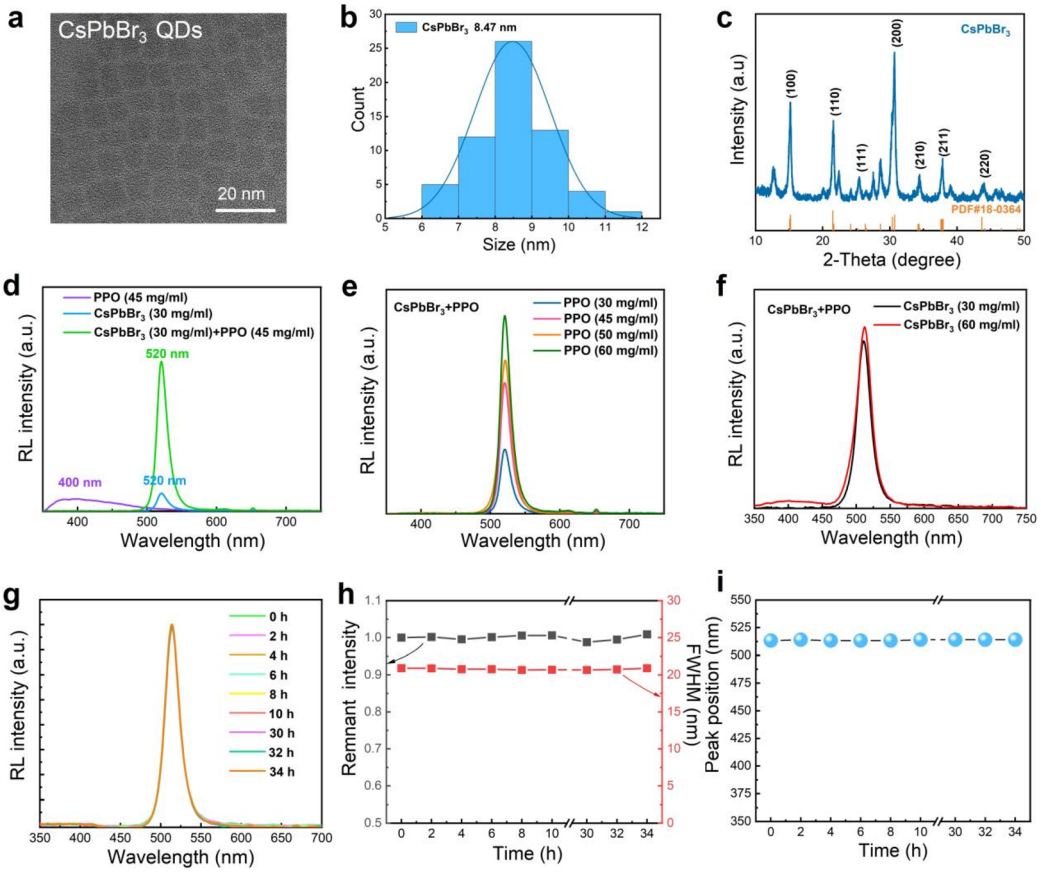

Fig. 2 (a–c) Transmission electron microscopy (TEM) image, particle size distribution, and X-ray diffraction (XRD) patterns of the $CsPbBr_3$ QDs, respectively. (d) Radioluminescence (RL) spectrum of PPO, $CsPbBr_3$ QDs, and $CsPbBr_3$ QDs/PPO. (e and f) RL spectrum of the $CsPbBr_3$ QDs/PPO as a function of PPO and $CsPbBr_3$ QD concentration, respectively. (g) RL spectrum of $CsPbBr_3$ QDs/PPO LSS under continuous X-ray illumination with 89 kV tube voltage. (h) RL peak intensity and FWHM of the $CsPbBr_3$ QDs/PPO LSS extracted from (g). (i) RL peak position of the $CsPbBr_3$ QDs/PPO LSS extracted from (g).

(Fig. S2b†). Fig. 2d shows a comparison of the RL spectra of the $CsPbBr_3$ QDs (30 mg ml^{-1}), PPO (45 mg ml^{-1}), and $CsPbBr_3$ QDs (30 mg ml^{-1})/PPO (45 mg ml^{-1}) scintillators. Compared with $CsPbBr_3$ QDs, the green emission intensity of $CsPbBr_3$ QDs/PPO is enhanced by approximately 8 times after adding PPO. Furthermore, the $CsPbBr_3$ QDs/PPO scintillator and pure $CsPbBr_3$ scintillator have the same RL peak positions, revealing that adding PPO does not significantly affect the emission energy of the $CsPbBr_3$ QDs while enhancing their RL intensity. The underlying reason is that those X-ray-induced electrons generated from PPO can transfer to the $CsPbBr_3$ QDs through surface hybridization and amplify the number of electrons in the $CsPbBr_3$ QDs (Fig. S3†), thus enhancing the RL from the QDs with the improved quantum yield. We further investigated how PPO contributed to the RL intensity of the $CsPbBr_3$ QDs/PPO hybrid scintillator by varying the concentration ratio of the $CsPbBr_3$ QDs and PPO. As shown in Fig. 2e, the RL emission intensity from the hybrid $CsPbBr_3$ QDs/PPO scintillator increases obviously with increasing PPO ($CsPbBr_3$ QDs: 30 mg ml^{-1}). We also carried out measurements by increasing the density of $CsPbBr_3$ QDs (PPO: 30 mg ml^{-1}). As the $CsPbBr_3$ QDs density increased from 30 to 60 mg ml^{-1}, there is a slight increase in the RL intensity (Fig. 2f).

The long-term stability of the X-ray detector was directly relevant to industrial applications. To evaluate the air stability of the encapsulated LSS, the PL evolution was measured with different storage times under ambient atmosphere (room temperature: 20–25 °C, humidity: 30–40%). As shown in Fig. S4,† the PL intensity retained 91% of the original value after 162 h. Furthermore, it was observed that the full width at half maximum (FWHM) value and peak position were almost unchanged, revealing the excellent moisture stability of the LSS. Radiation resistance is also a crucial feature of a scintillator. As illustrated in Fig. 2g–i, under a 34 h continuous X-ray irradiation (turn-off X-ray for 20 min within every 2 hours) under ambient conditions, the RL intensity, FWHM, and peak position exhibit tiny fluctuation, suggesting good radiation stability, which can be ascribed to that liquid scintillators have better resistance to the radiation damage as well as the protection of the OCA packaging. All the results demonstrated the superior stability of the $CsPbBr_3$/PPO LSS, laying a solid foundation for its wide application.

Fig. 3a shows the X-ray emission intensity of the $CsPbBr_3$ QDs/PPO LSS at different dose rates. It is found that the RL intensity increases linearly as the X-ray dose rate increases, as depicted in Fig. 3b. The detection limit is 79.1 μGy s^{-1}. Another key figure of merit of the LSS is the X-ray imaging ability. As a proof of concept, we employed our homemade X-ray imaging optical system (Fig. S5, ESI†) to explore the X-ray imaging potential of the $CsPbBr_3$ QDs/PPO LSS (Fig. 3c). The target objects were a circuit board, a ball-point pen, and a lead wire. The structural information of the circuit board, the metal spring inside the ball-point pen, and the lead wire was clearly observed, as seen in Fig. 3d. To evaluate the spatial resolution of the LSS, an X-ray image of a bar pattern phantom was taken (Fig. 3e). Fig. 3f shows the intensity variation along the yellow line in the X-ray images of the line patterns (inset of Fig. 3f

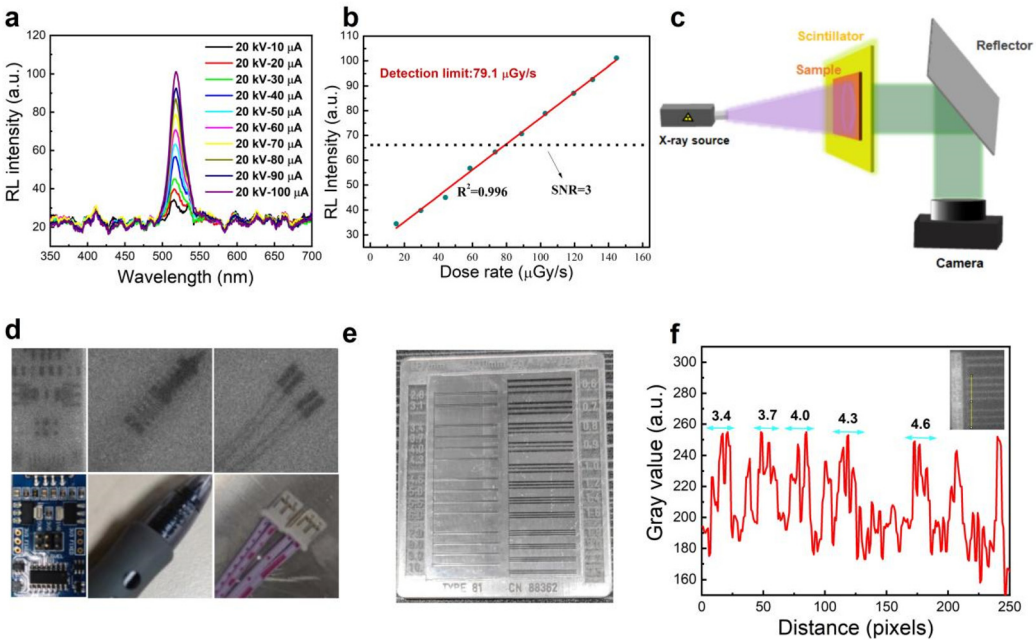

Fig. 3 (a) RL spectra of the $CsPbBr_3$ QDs/PPO LSS under X-ray with different dose rates. (b) Plotted RL intensity of the $CsPbBr_3$ QDs/PPO LSS dependent on the dose rate of X-rays. (c) Schematic graphic of the X-ray imaging system. (d) X-ray images and photographs of a circuit board, ball-point pen, and lead wire using the $CsPbBr_3$ QDs/PPO LSS. (e) Photograph of the X-ray resolution test pattern plate. (f) The graph of the gray value changes along the yellow line in the inset of f.

and Fig. S6†). Fig. S7† shows the modulation transfer function (MTF) for the $CsPbBr_3$ QDs/PPO LSS. The LSS had a detection resolution of at least 4.6 lp mm^{-1}. Such a detection resolution could meet the needs of dental diagnosis (1.6–3 lp mm^{-1}) and nondestructive inspection.

Thanks to the facile and easy fabrication process, this strategy also applies to other scintillators. Fig. 4a and b and c show the optical images of the Mn:$CsPbCl_3$ QDs/PPO liquid scintillator arrays under daylight and UV light excitation, respectively. Similar to the LSS based on $CsPbBr_3$ QDs/PPO, excellent uniformity and continuity were also observed for the Mn:$CsPbCl_3$ QDs/PPO. The Mn:$CsPbCl_3$ QDs were synthesized by the modified hot injection method (see Methods for details, $MnCl_2$/$PbCl_2$ = 2.5 : 1). Under natural light, Mn:$CsPbCl_3$ QDs are colorless and transparent (Fig. 4a and the inset image). Highly bright orange-yellow luminescence can be observed under 365 nm UV excitation (Fig. 4b and the inset image). The TEM image of the Mn:$CsPbCl_3$ QDs is shown in Fig. 4d. We can clearly see that Mn:$CsPbCl_3$ QDs are evenly dispersed in the whole field of vision, without the agglomeration phenomenon, and their shape is relatively regular, mainly manifested as cubic. The size of the synthesized Mn:$CsPbCl_3$ QDs sample shows a Gaussian distribution between 7 nm and 14 nm, while its average size is around 10.57 nm (Fig. S8†). Note that we chose Mn:$CsPbCl_3$ QDs instead of $CsPbCl_3$ QDs because the Mn doping strategy could greatly improve the PL quantum

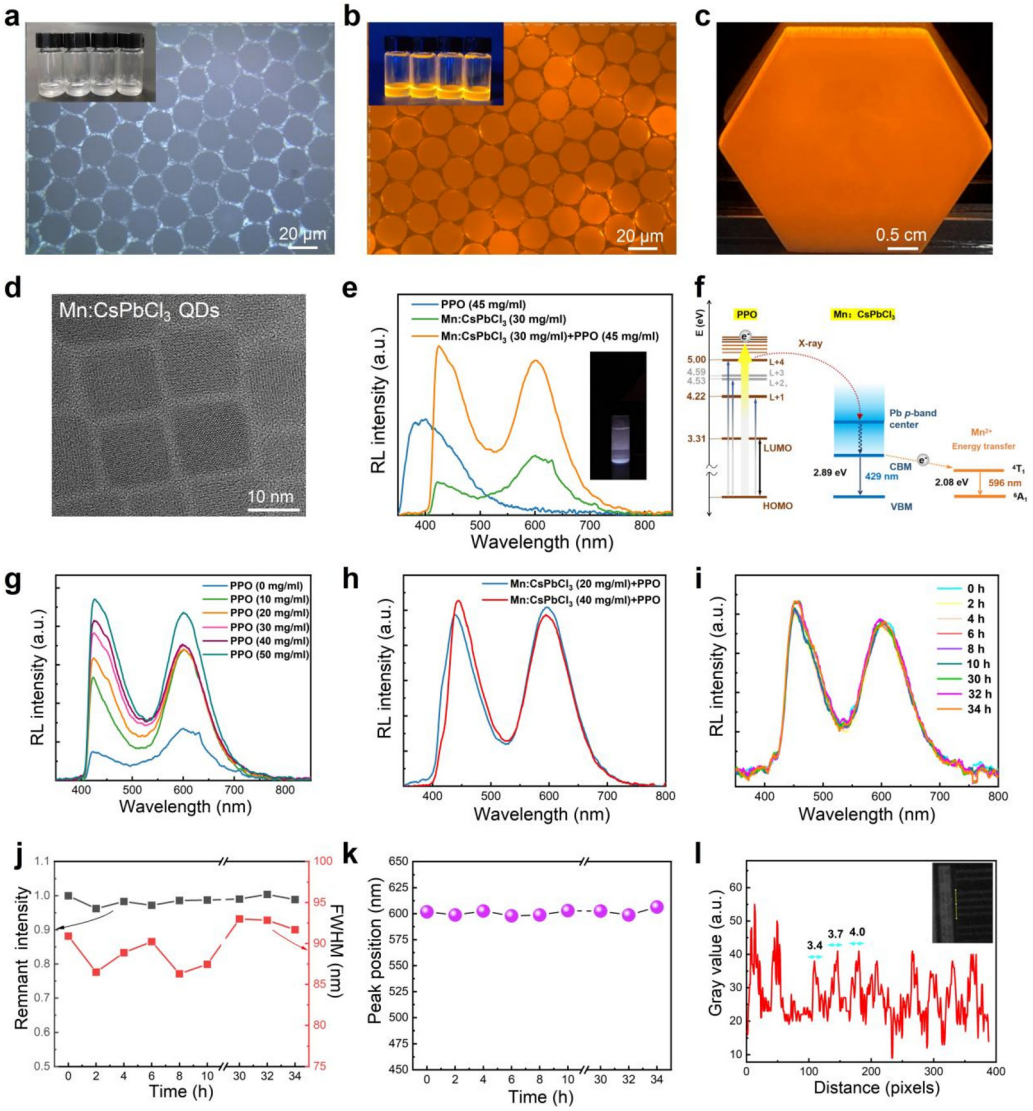

Fig. 4 (a and b/c) Optical image of the pixelated Mn:$CsPbCl_3$ QDs/PPO liquid scintillator arrays under daylight and UV light excitation, respectively. (d) TEM image of the Mn:$CsPbCl_3$ QDs, respectively. (e) RL spectrum of PPO, Mn:$CsPbCl_3$ QDs and Mn:$CsPbCl_3$ QDs/PPO. The inset of Fig. 4e shows the X-ray image of Mn:$CsPbCl_3$ QDs/PPO. (f) Energy level alignment for the proposed mechanism of enhanced RL in the Mn:$CsPbCl_3$ QDs/PPO scintillator. (g and h) RL spectrum of the Mn:$CsPbCl_3$ QDs/PPO as a function of PPO and Mn:$CsPbCl_3$ QD concentration, respectively. (i) RL spectrum of the Mn:$CsPbCl_3$ QDs/PPO LSS under continuous X-ray illumination with 89 kV turn-on voltage. (j) RL peak intensity and FWHM of the Mn:$CsPbCl_3$ QDs/PPO LSS extracted from (i). (k) RL peak position of the Mn:$CsPbCl_3$ QDs/PPO LSS extracted from (i). (l) The graph of the gray value changes along the yellow line in the inset of l.

yield due to the energy coupling between d orbitals and the host $CsPbCl_3$, as demonstrated in our previous work.[20] Herein, we further show that Mn:$CsPbCl_3$ QDs also display stronger emission under X-ray excitation. As shown in Fig. S9a,† $CsPbCl_3$ QDs emit blue fluorescence when excited by X-ray. In contrast, brighter white light emission was observed for Mn:$CsPbCl_3$, as shown in Fig. S9b.† This is because for $MnCl_2$/$PbCl_2$ = 2.5 : 1, Mn^{2+} does not completely replace Pb^{2+}, and some $CsPbCl_3$ QDs still exist. $CsPbCl_3$ and the Mn^{2+} luminescence center ($CsPbCl_3$: 423 nm, Mn:$CsPbCl_3$: 595 nm, Fig. S9c†) both show radioluminescence, and the two colors finally display white emission after mixing in a certain amount. The distinct emitting color of Mn:$CsPbCl_3$ QDs under UV and X-ray stimulation is possible because the energy coupling efficiency between the Mn d orbitals and $CsPbCl_3$ is relatively higher under UV excitation, as the PL intensity of $CsPbCl_3$ is much lower than that of the Mn luminescence center (Fig. S10a†). Further studies are needed to gain additional insights into this different coupling strength.

Fig. 4e presents the RL spectra of PPO, Mn:$CsPbCl_3$ QDs, and Mn:$CsPbCl_3$ QDs/PPO. It is also observed that the RL intensity of the hybrid Mn:$CsPbCl_3$ QDs/PPO scintillator is several times higher than that of the other two scintillators. Fig. 4f shows the proposed mechanism of enhanced RL in the Mn:$CsPbCl_3$ QDs/PPO scintillator. X-ray-induced electrons within PPO transfer to the $CsPbCl_3$ QDs through surface hybridization. More high-energy electrons engage in both the $CsPbCl_3$ CB–VB and Mn^{2+} d–d transition, contributing to the brighter emission. Similar to the $CsPbBr_3$ QDs/PPO system, the PPO concentration also plays an important role in the RL intensity of the hybrid Mn:$CsPbCl_3$ QDs/PPO system. The RL intensity continues to increase with the PPO concentration (Fig. 4g). Likewise, the RL emission is slightly changed as the Mn:$CsPbCl_3$ QDs density increases from 20 to 40 mg ml^{-1} (Fig. 4h). Next, we examined the long-term operational stability of the encapsulated Mn:$CsPbCl_3$ QDs/PPO LSS against X-ray illumination. The Mn:$CsPbCl_3$ QDs/PPO LSS retained its initial RL intensity after 34 h (Fig. 4i). Additionally, the FWHM and peak position showed negligible fluctuation (Fig. 4j and k), addressing a stable imaging capability. The Mn:$CsPbCl_3$ QDs/PPO LSS also exhibited good moisture stability, with the PL intensity retaining 88% of its initial intensity for 168 h (Fig. S10†). The spatial resolution and imaging ability of the Mn:$CsPbCl_3$ QDs/PPO LSS were also characterized, as shown in Fig. 4l and Fig. S11–S13,† respectively. A spatial resolution of 4.0 lp mm^{-1} was demonstrated. Furthermore, the detailed internal structure information of the circuit board, the ballpoint pen, and the lead wire was clearly obtained from the X-ray images, which provides a wide and potential application prospect for the medical inspection.

Discussion

This work provides a facile yet robust method to fabricate a high-performance LSS. Fig. S14a and S14b† show the optical images of the pixelated $CsPbBr_3$/PPO and Mn:$CsPbCl_3$/PPO LSS under UV light excitation after the second filling/packaging process, respectively. The LSS still shows good uniformity after the repeated filling/packaging process, demonstrating the reusable merit of the FOP substrate. We further evaluated the light yield of $CsPbBr_3$ QDs/PPO. A standard liquid scintillator (PPO + POPOP + toluene) was adopted for evaluating the light yield of $CsPbBr_3$/PPO. The RL spectra of standard LS, $CsPbBr_3$, $CsPbBr_3$/PPO were recorded, as shown in Fig. S15.† The results are provided in Table S2,† and the light yield of $CsPbBr_3$ (60 mg ml^{-1}) + PPO (60 mg ml^{-1}) is estimated to be 10.6 keV^{-1}. In addition, since the proposed method relies on the siphon principle, it significantly broadens the repertoire of usable materials and is highly versatile. For example, other perovskite QDs such as $FAPbX_3$, $CsSnX_3$, CdSe, and ZnS may be applicable to this method. We further investigated the effect of the thickness of the FOP on the light extraction efficiency of the LSS (Fig. S16–S18†). It can be due to the following reasons: (1) the penetration depth increases with the increase of X-ray tube voltage and (2) the self-absorption effect of the LSS, a 2 mm-thick LSS, possessed a higher (lower) light extraction efficiency than that of a 4 mm-thick LSS under X-ray conditions of 30 kV, 50 μA (60(70), 50 μA). Furthermore, the 4 mm-thick LSS showed higher light extraction efficiency than a 1 cm-thick LSS under X-ray conditions of 90 kV, 50 μA. Thus, we can design an LSS with an appropriate thickness for different application scenarios. Also, benefiting from the thickness-adjustable LSS, the energy-resolved radiation ability could be realized by integrating several LSSs with a varied thickness (Fig. S19†). Additionally, the LSS resolution could be further improved by reducing the pore diameter of LSS.

Conclusion

In summary, an X-ray LSS with a low dose rate (79.1 μGy s^{-1}) and high resolution (4.6 lp mm^{-1}) was constructed *via* the siphon effect. Furthermore, the $CsPbBr_3$/PPO LSS possessed excellent radiation tolerance (>34 h) and moisture stability (>160 h). This method works for a very broad spectrum of perovskite QDs ($CsPbBr_3$, $CsPbCl_3$, Mn:$CsPbCl_3$). The proposed strategy holds great potential for cost-effective, large-scale preparation and features easy maintenance and re-usability, thus offering a substantial impact on the development of X-ray imaging detectors for practical medical applications.

Methods

Chemicals

Cesium carbonate (Cs_2CO_3, 99.99%), lead bromide ($PbBr_2$, 99.99%), lead chloride ($PbCl_2$, 99.99%), manganese chloride ($MnCl_2$, ≧99%), 2,5-diphenyloxazole (PPO,99%), 1,4-bis(5-phenyl-2-oxazolyl)benzene (POPOP, 98%), oleic acid (OA, AR), 1-octadecene (ODE, 95%), oleylamine (OAm, 80%–90%), trioctylphosphine (TOP, 97%), methyl acetate (MeOAc, 99% anhy-

drous), and 1-bromonaphthalene (97%) were purchased from Aladdin and used without further purification.

Preparation of Cs-oleate

0.814 g of Cs_2CO_3, 40 ml of ODE, and 1.5 ml of OA were added to a three-necked round-bottom flask and heated under vacuum at 120 °C for 0.5 h. Next, the mixture was heated to a reaction temperature of 150 °C under a nitrogen atmosphere. The reaction was complete when the solution became clear.

Synthesis of $CsPbX_3$ (X = Cl or Br) nanocrystals and hybrid scintillators

First, 0.188 mmol of PbX_2 (X = Cl or Br), 10 ml of ODE, 1.5 ml of OA and 1.5 ml of OAm (additionally 1 ml of extra TOP was also added for $CsPbCl_3$ synthesis) were added and mixed in a three-necked round-bottom flask. The flask was heated to 100 °C under vacuum for 30 min and then to 150 °C (170 °C for $CsPbCl_3$) under a nitrogen atmosphere ($CsPbCl_3$ requires a reaction temperature of 170 °C) until the PbX_2 precursor was completely dissolved. Subsequently, 0.4 ml of the hot Cs-oleate precursor solution was quickly injected into the above reaction mixture. After 5 s of reaction, the flask was placed into ice bath apparatus. Finally, $CsPbX_3$ NCs were obtained, separated by 9000 rpm centrifugation for 5 min and dispersed in α-bremnaphthalene containing PPO for further use.

Synthesis of Mn-doped $CsPbCl_3$ perovskite nanocrystals and hybrid scintillators

First, 0.188 mmol of $PbCl_2$, 0.47 mmol of $MnCl_2$, 5 ml of ODE, 1.5 ml of OA, 1.5 ml of OAm, and 1 ml of TOP were mixed in a three-necked flask and dried under vacuum at 120 °C for 30 min. Then, the reaction temperature was raised to 170 °C under a nitrogen atmosphere, and 0.4 ml of hot Cs-oleate precursor was rapidly injected. After 10 s of reaction, the flask was quickly transferred into an ice bath for cooling. Finally, Mn-doped $CsPbCl_3$ perovskite nanocrystals were obtained by 9000 rpm centrifugation for 5 min and redispersed in α-bremnaphthalene containing PPO for further use.

Preparation of the liquid scintillation screen

Lead-containing hollow optical fibers are obtained *via* the industrial fiber drawing technology. The hot zone temperature and drawing speed are 800 °C and 1 m s^{-1}. FOPs with different thicknesses are obtained *via* the cutting technology. The liquid scintillation screen was prepared by filling the abovementioned solution of Mn-doped $CsPbCl_3$ QDs/PPO ($CsPbBr_3$ QDs/PPO) into the FOP through the siphon effect. The pore size of the lead-containing porous glass was 20 μm and the thickness was 2, 4 and 10 mm. For the filling and packaging process, OCA was first applied on the polyethylene glycolterephthalate film. Utilizing the siphon effect, the liquid perovskite scintillator was drawn into the optical fiber plate. Then, the PET films coated with OCA were adhered on both the upper and lower surfaces of the optical fiber plate. Next, ultraviolet light was used to rapidly cure the OCA adhesive. After the OCA adhesive is cured, the PET films were mechanically peeled off to obtain a pixelated array of the liquid perovskite.

RL and X-ray imaging

Radioluminescence (RL) was measured using a microfocal spot X-ray detector (ZM-X5600), and the voltage (10–90 kvp) and current (10–89 μA) of the electron tube were adopted during the test. Spectral data were acquired using a ∅200 μm core fiber and a spectrometer (QE65Pro) with a wavelength range of 200–1000 nm. X-ray excitation luminescence photographs were acquired using a cooled high-sensitivity camera (PM001). The concentration used in the scintillation screen was $CsPbBr_3$ (60 mg ml^{-1})/PPO (60 mg ml^{-1}) and Mn:$CsPbCl_3$ (40 mg ml^{-1})/PPO (60 mg ml^{-1}). The concentration for the standard liquid scintillator is PPO (4 mg ml^{-1}) + POPOP (0.1 mg ml^{-1}) + toluene (1 ml). For X-ray imaging, the thickness of the LSS is 4 mm.

Data availability

The data that support the findings of this study are available from the corresponding authors upon reasonable request.

Code availability

The code that supports the plots within this study is available from the corresponding authors upon reasonable request.

Conflicts of interest

There are no conflicts to declare.

Acknowledgements

This work was partially supported by the Shenzhen Basic Research Grant (GJHZ20200731095601004, JCYJ20200109114801744, JCYJ20210324115406019), the Guangdong Basic and Applied Basic Research Foundation (2023A1515030113), and the Youth Innovation Promotion Association, Chinese Academy of Sciences, China (2023375). This work was also supported by the National Natural Science Foundation of China (52002393, 52173243) and the SIAT-CUHK Joint Laboratory of Photovoltaic Solar Energy. This work was also supported by the Singapore Ministry of Education Academic Research Fund Tier 2 (MOE2019-T2-2-127 and MOE-T2EP50120-0002), the Singapore Ministry of Education Academic Research Fund Tier 1 (RG62/22), A*STAR under AME IRG (A2083c0062), and A*STAR under IAF-ICP Programme I2001E0067 and the Schaeffler Hub for Advanced Research at NTU. This work was supported by the IDMxS (Institute for Digital Molecular Analytics and Science) by the Singapore Ministry of Education under the Research Centres

of Excellence scheme. This work was also supported by the NTU-PSL Joint Lab collaboration.

References

1 H. Grassmann, H. Moser and E. Lorenz, Properties of CsI (Tl)-Renaissance of an old scintillation material, *Nucl. Instrum. Methods Phys. Res., Sect. A*, 1985, **228**(2–3), 323–326.
2 W. Mengesha, T. Taulbee, B. Rooney, *et al.*, Light yield non-proportionality of CsI (Tl), CsI (Na), and YAP, *IEEE Trans. Nucl. Sci.*, 1998, **45**(3), 456–461.
3 C. W. Van Eijk, Inorganic scintillators in medical imaging, *Phys. Med. Biol.*, 2002, **47**(8), R85.
4 S. He, S. Chen, D. Li, *et al.*, High affinity to skeleton rare earth doped nanoparticles for near-infrared II imaging, *Nano Lett.*, 2019, **19**(5), 2985–2992.
5 P. Yang, C. D. Harmon, F. P. Doty, *et al.*, Effect of humidity on scintillation performance in Na and Tl activated CsI crystals, *IEEE Trans. Nucl. Sci.*, 2014, **61**(2), 1024–1031.
6 R. Yasuda, M. Katagiri and M. Matsubayashi, Influence of powder particle size and scintillator layer thickness on the performance of Gd_2O_2S: Tb scintillators for neutron imaging, *Nucl. Instrum. Methods Phys. Res., Sect. A*, 2012, **680**, 139–144.
7 Q. Chen, J. Wu, X. Ou, *et al.*, All-inorganic perovskite nanocrystal scintillators, *Nature*, 2018, **561**(7721), 88–93.
8 J. Liu, B. Shabbir, C. Wang, *et al.*, Flexible, printable soft–X–ray detectors based on all–inorganic perovskite quantum dots, *Adv. Mater.*, 2019, **31**(30), 1901644.
9 K. Abdel-Latif, F. Bateni, S. Crouse, *et al.*, Flow synthesis of metal halide perovskite quantum dots: from rapid parameter space mapping to AI-guided modular manufacturing, *Matter*, 2020, **3**(4), 1053–1086.
10 B. Yang, L. Yin, G. Niu, *et al.*, Lead–Free Halide Rb_2CuBr_3 as Sensitive X–Ray Scintillator, *Adv. Mater.*, 2019, **31**(44), 1904711.
11 Q. Xu, S. Zhou, J. Huang, *et al.*, Ultra-flexible and highly sensitive scintillation screen based on perovskite quantum dots for non-flat objects X-ray imaging, *Mater. Today Phys.*, 2021, **18**, 100390.
12 X. Yang, C. Valenzuela, X. Zhang, *et al.*, Robust integration of polymerizable perovskite quantum dots with responsive polymers enables 4D-printed self-deployable information display, *Matter*, 2023, **6**(4), 1278–1294.
13 Y. Zhao, E. Brun, P. Coan, *et al.*, High-resolution, low-dose phase contrast X-ray tomography for 3D diagnosis of human breast cancers, *Proc. Natl. Acad. Sci. U. S. A.*, 2012, **109**(45), 18290–18294.
14 M. Simon, K. J. Engel, B. Menser, *et al.*, Challenges of pixelated scintillators in medical X-ray imaging, *Nucl. Instrum. Methods Phys. Res., Sect. A*, 2008, **591**(1), 291–295.
15 H. Chen, M. Gu, X. Liu, *et al.*, Effect of CsI (Tl) micro-conical-frustums on the performance of the pixelated CsI (Tl) scintillation screen in X-ray imaging, *Nucl. Instrum. Methods Phys. Res., Sect. A*, 2019, **921**, 18–21.
16 H. Wang, J. X. Wang, X. Song, *et al.*, Copper Organometallic Iodide Arrays for Efficient X-ray Imaging Scintillators, *ACS Cent. Sci.*, 2023, **9**(4), 668–674.
17 H. Li, H. Yang, R. Yuan, *et al.*, Ultrahigh Spatial Resolution, Fast Decay, and Stable X-Ray Scintillation Screen through Assembling $CsPbBr_3$ Nanocrystals Arrays in Anodized Aluminum Oxide, *Adv. Opt. Mater.*, 2021, **9**(24), 2101297.
18 X. Zhao, T. Jin, W. Gao, *et al.*, Embedding $Cs_3Cu_2I_5$ Scintillators into Anodic Aluminum Oxide Matrix for High-Resolution X-Ray Imaging, *Adv. Opt. Mater.*, 2021, **9**(24), 2101194.
19 S. Cho, S. Kim, J. Kim, *et al.*, Hybridisation of perovskite nanocrystals with organic molecules for highly efficient liquid scintillators, *Light: Sci. Appl.*, 2020, **9**(1), 156.
20 F. Sui, M. Pan, Z. Wang, *et al.*, Quantum yield enhancement of Mn-doped $CsPbCl_3$ perovskite nanocrystals as a luminescent down-shifting layer for CIGS solar cells, *Sol. Energy*, 2020, **206**, 473–478.